journal of the mechanical behavior of biomedical materials 141 (2023) 105760

Contents lists available at ScienceDirect

Journal of the Mechanical Behavior of Biomedical Materials

journal homepage: www.elsevier.com/locate/jmbbm

Research paper

Mechanical characterization of miniaturized 3D-printed hydroxyapatite parts obtained through vat photopolymerization: an experimental study

Luca D'Andrea [a], Dario Gastaldi [a], Francesco Baino [b], Enrica Verné [b], Giulia Saccomano [c,d], Lorenzo D'Amico [c,e], Elena Longo [c], Martin Schwentenwein [f], Pasquale Vena [a,*]

[a] Department of Chemistry, Materials and Chemical Engineering "Giulio Natta", Laboratory of Biological Structure Mechanics (LaBS) - Politecnico di Milano, Piazza Leonardo da Vinci 32, 20133, Milano, Italy
[b] Institute of Materials Physics and Engineering, Department of Applied Science and Technology - Politecnico di Torino, 10129 Torino, Italy
[c] Elettra-Sincrotrone Trieste S.C.p.A., Strada Statale 14 – km 163,5 in AREA Science Park, 34149, Basovizza, Italy
[d] Department of Engineering and Architecture - University of Trieste, Via A. Valerio 6/1, Trieste, Italy
[e] Department of Physics - University of Trieste, Via A. Valerio 2, 34127 Trieste, Italy
[f] Lithoz GmbH, Mollardgasse 85a/2/64-69, 1060, Wien, Austria

ARTICLE INFO

Keywords:
Hydroxyapatite
Micro-bending tests
Computed micro-Tomography
Vat photopolymerization
Stereolithography

ABSTRACT

Hydroxyapatite is one of the materials of choice for tissue engineering bone scaffolds manufacturing. Vat photopolymerization (VPP) is a promising Additive Manufacturing (AM) technology capable of producing scaffolds with high resolution micro-architecture and complex shapes. However, mechanical reliability of ceramic scaffolds can be achieved if a high fidelity printing process is obtained and if knowledge of the intrinsic mechanical properties of the constituent material is available. As the hydroxyapatite (HAP) obtained from VPP is subjected to a sintering process, the mechanical properties of the material should be assessed with specific reference to the process parameters (e.g. sintering temperature) and to the specific characteristic size of the microscopic features in the scaffolds. In order to tackle this challenge the HAP solid matrix of the scaffold was mimicked in the form of miniaturized samples suitable for ad hoc mechanical characterization, which is an unprecedented approach. To this purpose small scale HAP samples, having a simple geometry and size similar to that of the scaffolds, were produced through VPP. The samples were subjected to geometric characterization and to mechanical laboratory tests. Confocal laser scanning and Computed micro-Tomography (micro-CT) were used for geometric characterization; while, micro-bending and nanoindentation were used for mechanical testing. Micro-CT analyses have shown a highly dense material with negligible intrinsic micro-porosity. The imaging process allowed quantifying the variation of geometry with respect to the nominal size showing high accuracy of the printing process and identifying printing defects on one specific sample type, depending on the printing direction. The mechanical tests have shown that the VPP produces HAP with an elastic modulus as high as approximately 100 GPa and flexural strength of approximately 100 MPa. The results of this study have shown that vat photopolymerization is a promising technology capable of producing high quality HAP with reliable geometric fidelity.

1. Introduction

Design of patient specific Bone Tissue Engineering (BTE) scaffolds is a promising approach to the clinical treatment of critical bone defects; their capability to promote new bone formation by patient's own cells on a solid load bearing structure can substantially help in restoring organ functionality in a short rehabilitation time (Bigham et al., 2020; Campana et al., 2014). Design and manufacturing of BTE scaffolds is a complex task that has to address different requirements and constraints. It is well known that a BTE scaffold architectural design has to guarantee structural integrity in terms of stiffness and strength of the device, to account for tissue conditions in the hosting anatomical environment so to limit stress shielding and avoid insufficient fluid flow as well as to maximize bone formation and biocompatibility.

* Corresponding author.
E-mail addresses: luca.dandrea@polimi.it (L. D'Andrea), dario.gastaldi@polimi.it (D. Gastaldi), francesco.baino@polito.it (F. Baino), enrica.verne@polito.it (E. Verné), giulia.saccomano@elettra.eu (G. Saccomano), lorenzo.damico@elettra.eu (L. D'Amico), elena.longo@elettra.eu (E. Longo), mschwentenwein@lithoz.com (M. Schwentenwein), pasquale.vena@polimi.it (P. Vena).

https://doi.org/10.1016/j.jmbbm.2023.105760
Received 26 June 2022; Received in revised form 15 January 2023; Accepted 4 March 2023
Available online 6 March 2023

Among potential materials for scaffold manufacturing, hydroxyapatite (HAP) is one of the most frequently selected due to its similarity to the bone mineral constituents and ability to promote osteo-integration and offering good biocompatibility (Dorozhkin and Epple, 2002). The above mentioned properties foster the development of HAP based materials as bone fillers, spacers or as coatings able to improve stability of the implants through enhanced bone growth (Szcześ et al., 2017; Goloshchapov et al., 2019). The application of the HAP in a more demanding clinical context such as the case of bone substitution in critical size bone defects was considered thanks to the improvements of manufacturing process that allowed creating micro-structured HAP materials with interconnected (Kumar et al., 2019) or hierarchical porosity (Kim et al., 2022).

Additive Manufacturing (AM) technologies offer a wide selection of suitable techniques to generate scaffold having complex architectures which can be purposely designed to meet specific requirements (Ghorbani et al., 2020; Zocca et al., 2015; Zeng et al., 2018; Jiao et al., 2022). Most AM technologies offers printing capability allowing for accurate and reliable control on the printed structures even for complex architectures; in particular, lithography-based methods allows achieving the highest spatial resolution among the currently-available AM strategies (less than 50 μm) (Paterlini et al., 2021; Baino et al., 2022).

The mechanical reliability of the scaffolds is one of the key pillars in the scaffold design, and the capability of predicting scaffold macroscopic stiffness and strength is of primary importance in an effective design process (Chen et al., 2014). To this purpose the knowledge of the mechanical properties of the constituent materials is needed. In particular, the elastic properties, strength and toughness are the main mechanical parameters feeding the in-silico models of scaffold devices which aim at determining the overall (macroscopic) mechanical properties (see for example Farina et al. (2021), Entezari et al. (2016)). When the constituent materials exhibit a brittle stress–strain response, the reliability of the numerical models aiming at predicting the overall mechanical response of the scaffolds is even more important (Ritchie, 2011). To this purpose, the properties of the materials should be determined accounting for the peculiarity of the specific device; in particular, the characteristic size of the microstructure, as well as the whole manufacturing process should be allowed for. Sintered ceramic materials will exhibit intrinsic nano or micro-scale porosity and flaws as well as grain boundaries the size of which might be of similar order of magnitude of the scaffold architectural features. Furthermore, different technological parameters like sintering temperature or cooling rates would affect the final properties of the materials. Ideally, assessing the intrinsic material properties would be essential on samples produced by the same technology, using the same process parameters as that used in scaffold manufacturing and exhibiting the same characteristic size of the micro-architectural features of the scaffolds. The knowledge and investigation of these aspects are still missing in the literature, especially with reference to the HAP material and to the vat photopolymerization (VPP).

This paper aims at filling this gap by developing an experimental setup for mechanical tests on small HAP samples fabricated by VPP.

In this work, a previously developed experimental setup suitable for the mechanical characterization of small bone samples (Gastaldi et al., 2020) was improved to perform the mechanical characterization of miniaturized HAP samples obtained by VPP; for this purpose, confocal laser scans, computed micro-Tomography scans and nanoindentation tests were used to complement the mechanical tests. The processing parameters used for the fabrication of bulk samples are the same as those used for the fabrication of bone-like scaffolds in a previous work (Baino et al., 2022); in this regard, the characteristic size of the samples (few hundreds of micrometers) corresponds to the typical size of the micro-architectural features of porous bone scaffolds.

Table 1
Geometric size of samples produced through vat photopolymerization.

Type	L [mm]	w [mm]	t [mm]	R [mm]	t_{res} [mm]
beams	10	1	0.4	–	–
beams w. notch	10	1	0.4	0.2	0.2
cantilever	7	1	0.4	–	–

2. Materials and methods

2.1. Material samples

In this work, synthetic hydroxyapatite obtained through VPP method has been characterized. To this purpose, small-sized samples for bending tests have been manufactured. The characteristics of the printing system as well as the slurry composition/properties and multistage thermal treatment (final sintering at 1275 °C for 2 h) have been described in a previous work focused on the fabrication of bone-like HAP scaffolds (Baino et al., 2022). Details on the HAP miniaturized samples are here summarized. All samples were printed using a layer thickness of 25 μm in the green state. The used HAP suspension was LithaBone 480 (Lithoz GmbH, Vienna, Austria) and had a solids loading of 40 $vol\%$. Solidification of the individual layers was achieved by exposing the suspension to blue light with a peak wavelength of 460 nm. The corresponding exposure energy was 150 mJ/cm^2 for each layer. After printing, the excess suspension was removed using LithaSol 30 (Lithoz GmbH, Vienna, Austria) and pressurized air and the 3D printed green parts were thermally post-processed (multi-stage debinding and sintering with maximum temperature of 1300 °C for 2 h) to develop the final ceramic properties.

As printing accuracy in terms of geometrical regularity of the produced samples was not known a-priori, three different kinds of samples have been produced (number of samples is reported in round brackets): (i) simple beams with rectangular cross section ($N = 30$), (ii) beams with rectangular cross sections with circular notch ($N = 30$) and (iii) cantilevers ($N = 30$). Samples types (i) and (iii) where designed with the purpose to determine elastic modulus of the material and flexural strength, while sample type (ii) was only used for strength assessment. The nominal geometric characteristics of 3D-printed samples are reported in Table 1 in which L is the sample major length, w and t are width and thickness of samples, while R and t_{res} are the round notch radius and residual thickness at the notch in notched beams (see Fig. 1).

Because of the layerwise built-up of the green part the shrinkage during sintering was slightly anisotropic with a linear shrinkage of 22.5% in x,y-direction and 24.8% in z-direction. Consequently, the thickness of an individual layer after sintering was approximately 19 μm. The beams (with and without notch) were printed in an orientation in which the narrow side ($L \times t$) was attached to the building platform, the cantilevers were printed standing upright with the small rectangular side attached to the building platform.

2.2. Micro-CT characterization

Micro-CT studies for the characterization of material compactness and the assessment of intrinsic micro-porosity were performed at the SYRMEP (SYnchrotron Radiation for MEdical Physics) beamline (Dullin et al., 2021) of the Elettra Synchrotron Facility (Trieste, Italy) using propagation-based phase-contrast method.

The white beam setup with a 1.5 mm Silicon + 1 mm Aluminum filters was used with electron ring operating at 2.4 GeV, resulting in an average X-ray beam energy of 28 keV. Each scan was acquired with 1800 projections over 180 degrees by a water-cooled 16-bit sCMOS camera (Hamamatsu C11440-22C-Flash4.0 v2). The samples were measured at a detector-to-sample-distance (DSD) of 150 mm with a pixel size of 0.9 μm. The exposure time was 500 ms. The SYRMEP Tomo Project software was used to reconstruct the images (Brun et al., 2015). The

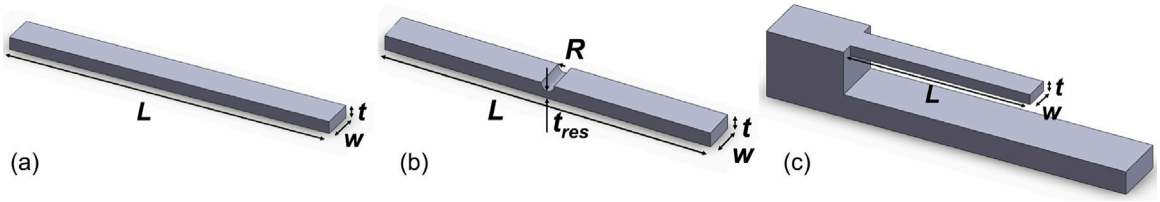

Fig. 1. Geometry of the three types of samples: (a) simple beams; (b) beams with a circular notch; (c) cantilever.

single distance phase retrieval pre-processing algorithm (Paganin et al., 2002) was used with delta over beta of 20 (DSD 150 mm). Filtered back projection was applied for image reconstruction using the Shepp–Logan filter.

In order to get quantitative information on the intrinsic porosity of the beams, 32-bit images were first converted to 8-bit images, then binarized in Fiji software (https://imagej.net/software/fiji/) following a three-step procedure as follows. First, a sub-region of the whole image was selected in order to exclude peaks due to the phase contrast artefacts occurring on the corners of the beam. Second, starting from the histogram of the grey levels (GLs) defined on the above selected sub-region, GLs were rescaled by setting the minimum GL at the right tail of the background peak and the maximum GL at the middle of the solid phase (HAP) peak (see Fig. 2). Third, the Otsu algorithm was used to binarize the image (Otsu, 1979).

3D object counter built-in Fiji software is applied on the inverted image with the purpose to characterize the porosity. The 3D object counter tool provides for each identified object its volume, and position. Pore diameter is estimated by making the simplifying assumption that voids are nearly spherical.

2.3. Geometric measures of the printed samples

As the VPP production process includes a sintering phase at high temperature and subsequent cooling phase at room temperature, shrinkage and shape variation with respect to the nominal geometry are expected in the final product. Laser scanning imaging is taken for all samples with the purpose to take accurate measurement of each sample and to quantify differences with respect to the nominal geometry; this step has also allowed discarding samples with unacceptable distortions.

Before each test, all samples were subjected to confocal laser scanning microscopy (LEXT OLS4100, Olympus, Tokyo, Japan). A 5X objective was used with a spatial resolution of 2.5 μm in the x-y plane; resolution of 10 μm along the z direction was achieved during confocal imaging.

As the field of view was smaller than the whole sample size, a stitching procedure has been used with the purpose to fit the entire sample in one single image. The confocal laser scanning microscope provided two types of data: (i) an image of the sample and (ii) a quantitative 3D topography of the scanned surface. The height data representing the 3D topography were exported for further analysis (see below).

A representative example of the image obtained from laser intensity data for one cantilever is reported in Fig. 3.

For beam samples, one top view scan was performed with the purpose to determine width (w) and thickness (t) (see Fig. 4). For notched beam samples, one top view scan is performed with the purpose to determine width (w) and thickness (t) as well as the thickness of notch (t_{res}) and radius (R).

In order to quantify beam thickness, the height data obtained through confocal lases microscopy were used. The procedure was as follow: in the first place, a region of interest (ROI) containing the sample and part of the background was cropped from the whole image. The height data are typically characterized by a two narrow peaks histogram, being the two peaks corresponding to the average height of the sample and to the background. The average value of all height data is located in between the two peaks and it is used as a threshold to identify the point data belonging to the sample. The average values of height of samples $\bar{t}_s$ and the average height of the background $\bar{t}_b$ were identified. The beam thickness t was determined as $t = \bar{t}_s - \bar{t}_b$.

The width w of each sample was identified through the following procedure. First the boundaries of the sample contour were identified by taking the spatial gradient of the height data; being the sample of a rectangular shapes, two short and two long boundaries were identified. One of the long boundaries of the rectangular area of the sample was selected: for each point of this boundary, a bundle of straight lines passing through the same point (x_p, y_p) were defined with m identifying the slope of each line ($y = y_p + m(x - x_p)$); than the intercept point of each line of the bundle with the second long boundary was identified and the distance between the center of the bundle and the intercept point was calculated as a function of m ($d(m)$). The width $w(x_p)$ at that particular location (x_p) along the boundary was given by $w(x_c) = min_m d(m)$. The width of the whole sample (w) was obtained as the average values for all x_p location on the selected long boundary.

In notched beams, the geometric parameters t_{res} and notch radius R were also measured trough the height data of the confocal laser scanning. The t_{res} was obtained as average values of the lowest thickness in the region of interest identified in the area of the notch. The notch radius was calculated by taking three parallel height profiles across the notch and fitting a circle on the three profiles. The notch radius has been assumed as the average value of the radii obtained in the three profiles.

For simple and notched beams the in-plane deformation induced by the sintering process was also measured on the x-y image as the length (c) reported in Fig. 4. For each cantilever sample, two scans are carried out. The top view scan which are used to determine the width (w) and length (L) of the samples, while the side view scan will be used to determine the thickness (t) by using the same procedure above described.

2.4. Micro-bending tests

Micro-bending tests have been performed by using an in-house developed tester (Gastaldi et al., 2020) featuring a 25 mm translational stage, a DC gear motor and a high resolution encoder (M-112.2DG, 50 nm resolution encoder, Physic Instrumente, Karlsruhe, Germany). In particular, three-Points Bending Tests (3PBT) and four-Points Bending Tests (4PBT) were performed. Cylindrical external supports were mounted on the moving component of the system, the distance between the two support was 8 mm, while the loading component (one point load for the 3PBT and two points load for the 4PBT) was connected to the fixed miniature load cell (Model 31, range 5 N, accuracy ±0.25% FC, Honeywell, Charlotte, NC). The loading nose for the 4PBT had emi-cylindrical shapes at a distance of 4 mm (inner span for the 4PBT; the outer span was 8 mm). The overall compliance of the loading apparatus was calibrated in Gastaldi et al. (2020).

Simple beam samples were subjected to 3PBT ($N = 25$) and to 4PBT ($N = 5$) by driving the displacement of the moving stage at a displacement rate of 0.1 μm/s up to sample failure. Force displacement data were collected for all tests for further post-processing.

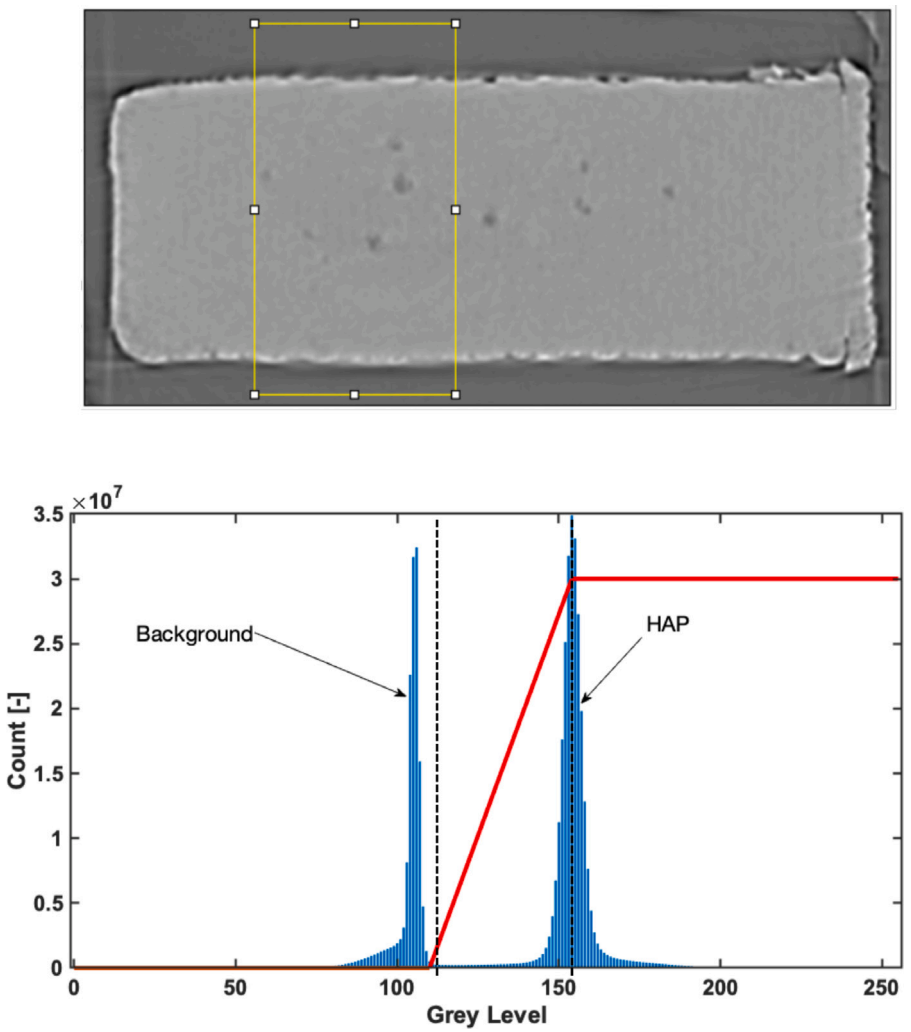

Fig. 2. Top panel: definition of the subregion to define the rescaled range of grey-scale (yellow rectangle); Bottom panel: grey-scale histogram on the ROI and definition of the rescaled range of the grey-levels; dotted lines defines the upper and lower boundaries of the new rescaled range.

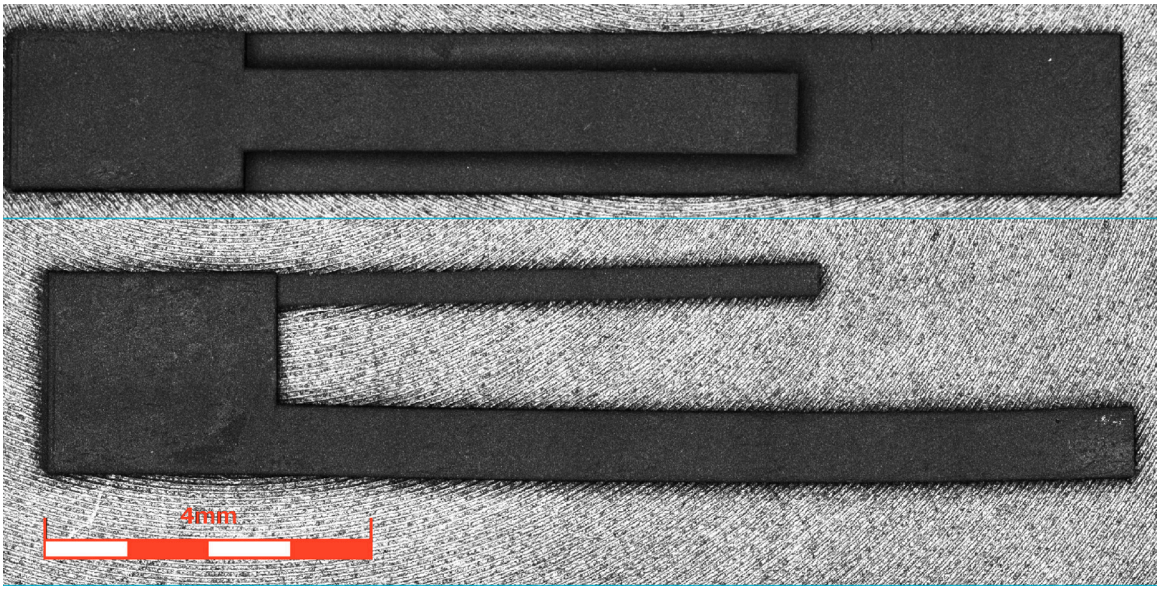

Fig. 3. Two views of one cantilever sample: laser intensity image.

Fig. 4. Definition of the deviation from rectilinear geometry for beam samples; top panel: laser intensity image; bottom panel: top surface mask (yellow pixels) obtained through the height laser data; definition of the deviation c is reported.

All tests were carried out under the optical stereo-microscope (SZ51, Olympus, Tokyo, Japan), equipped with a Camera (IDS GE camera UI-5490SE-C-HQ, IDS Imaging Development Systems GmbH, Obersulm, Germany), for continuous monitoring of the sample during the test.

Cantilever samples were subjected to loading by using the same loading nose used for 3PBT; the lower base of the samples were simply supported at the base of the translational stage. The distance between the loading point and the clamped end of the cantilever was approximately 4 mm and was measured for each experiments by inspecting a calibrated microscope image taken at the time of the test.

Elastic modulus of the material (E_f) was obtained through standard beam theory from 3PBT and 4PBT (simple beams) and cantilever samples; force displacement slope in the elastic regime was determined by best fitting the experimental data including experimental data points in the fitting range until $R^2 > 0.99$ was achieved.

Flexural strength of the material was obtained by calculating the maximum stress in the cross section having the maximum bending moments for the simple beams (3PBT and 4PBT) and for the cantilever samples. The maximum bending moment was determined at the failure load of all samples.

The flexural strength was also determined from beams with notch subjected to 4PBT. In this latter case, a stress concentration was achieved at the apex of the semi-circular notch. In order to estimate the strength, a finite element model has been made simulating the 4PBT on a beam with the notch. Different notch radii (R) and different notch thickness (t_{res}) have been modeled. The maximum stress was determined after a suitable mesh convergence analysis was performed.

The finite element model was used with the purpose to determine the following relation:

$$\sigma_{max} = K(R, t_{res}) \cdot F_{failure} \tag{1}$$

in which R is the notch radius and t_{res} is the residual thickness of the sample.

The tensile strength for the ith sample (σ^i_{max}) was determined as:

$$\sigma^i_{max} = K\left(R_i, t^i_{res}\right) \cdot F^i_{failure} \tag{2}$$

where R_i and t^i_{res} are related to the relevant samples obtained through imaging of the sample before the test (see Section 2.3).

Strength data obtained from notched beams and cantilever were collected together for the estimation of the Weibull modulus. As done in Baino et al. (2022), the Weibull modulus m was obtained as the slope of the linear fit of

$$\ln\left(\ln\left(\frac{1}{1-F}\right)\right) = m\ln(\sigma) - m\ln\left(\sigma_0\right) \tag{3}$$

in which $F = \frac{j-0.5}{N}$ is the probability of failure at a given stress level σ; j is the specimen rank in ascending order of failure stresses and N is the total number of samples and σ_0 is the Weibull scale parameter.

2.5. Nanoindentation tests

Three sample fragments obtained after bending failure were prepared for further nanoindentation tests.

The samples were embedded in epoxy resin and subjected to mirror polishing until a surface roughness of $R_a = 55$ nm $\pm$ 23 nm and $R_q = 87$ nm $\pm$ 29 nm was achieved. The heterogeneous nature of the surface (presence of post-sintering residual small pores) did not allow us to obtain smoother surfaces.

Nanoindentation tests were performed on Nanotest Platform 3 (MicroMaterials) at controlled temperature of 28 °C using a Berkovich indenter. Load controlled indentation tests were performed at 10, 50, 100, 200 mN with 25 repetitions for each load level. Cross talk was avoided by setting a 50 μm interspace between consecutive indentations. As the expected maximum penetration depth was lower than 1 μm, the 50 μm interspace was deemed to be sufficiently large. Loading and unloading rates were 2.5 mN/s and 5 mN/s, respectively; holding times of 3 s at the maximum load was applied (Shahgholi et al., 2016). Before the end of the test, the load was held constant for 30 s at 10% of the maximum load; the measured displacement drift was used for the thermal drift compensation during post-processing. Diamond Area Functions (DAFs) and compliance values were calibrated on standard samples (fused silica) with standard procedures.

All force–displacement nanoindentation data were analyzed by means of the Oliver–Pharr theory. Unloading curves were interpolated between 95% and 50% of the maximum load for slope (S) calculation. The nanoindentation modulus (M) was determined by standard approach:

$$\frac{1}{E^*} = \frac{1-\nu_i^2}{E_i} + \frac{1}{M} \tag{4}$$

$$\frac{1}{M} = \frac{1-\nu_s^2}{E_s} \tag{5}$$

in which $E_i = 1141$ GPa and $\nu_i = 0.07$ are the mechanical properties of the diamond indenter.

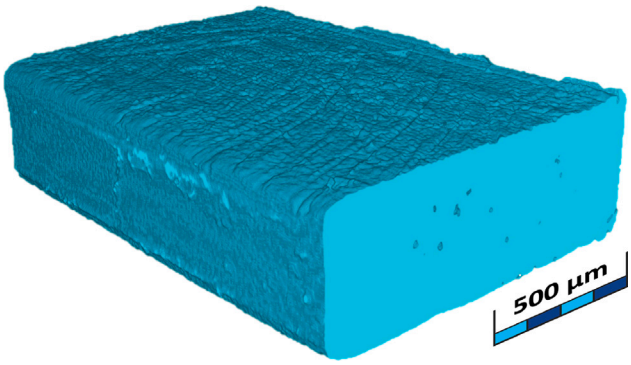

Fig. 5. Three-dimensional reconstruction of a portion of simple beams, in the cross section porosity is clearly shown.

2.6. Statistical treatment of measured data

The collected data underwent to statistical tests in order to identify significant difference between measures (reference p-value was set to 0.05). In particular, the Mann Witney U test has been performed to compare: (i) the indentation modulus at different indentation loads; (ii) the average elastic modulus obtained through indentation and that obtained through the bending of cantilever samples and (iii) the average strength obtained through the bending of cantilever and notched beams.

3. Results

3.1. Micro-CT analyses

Micro-CT scans on a simple beam sample have shown a highly dense material with isolated porosity; Fig. 5 shows a three-dimensional reconstruction of the central portion of a beam (size $2\times1\times0.4$ mm). On the cross section (approx. 1 mm $\times$ 0.4 mm), isolated pores are visible.

Fig. 6 shows a histogram of the pore diameters found in the region of interest (the whole domain of Fig. 5); pore diameter spanned from approximately 2 µm to 25 µm. In this histogram single pixel porosity have been considered as noise, therefore they were not included in the probability density plot. Few pores larger than 25 µm were also found, these were an artefact of the micro-CT reconstruction and, thus have been left out of this analyses. As two peaks were roughly identified in the histogram representation, a mixture of two normal distributions was used to fit the probability density function. The two peaks were identified as centered at 3.7 µm and 12.7 µm; the overall average pore diameter was 9.8 µm. The overall porosity was as low as 0.35%, indicating that the pores were isolated at large mutual distance.

Porosity was not uniformly distributed through the cross section of the beams; Fig. 7 shows spatial distribution of all pores in the volume projected on the cross section; the figure shows that the smallest pores were mainly located on the boundary of the sample, while larger pores are more concentrated in the core of the sample.

3.2. Geometrical features of the samples

Confocal laser scanning allowed us to determine the size of each sample before destructive mechanical tests. The geometrical parameters obtained were used to determine elastic modulus and flexural strength of each sample. Table 2 shows that the printing process was sufficiently accurate as average values of the final size of samples was close to the nominal one with a maximum error of about 100 µm for the t_{res} parameter which was, however, the thinnest nominal size in the design and the technologically most difficult to attain. With the exception of the t_{res} parameters, the remaining geometrical sizes of the printed samples were accurate within the 17% error found on the t parameter for the simple beams. The sintering process produced deviations of the rectilinear long edge of simple and notched beams (see definition of the geometric parameter in Fig. 4). The simple beams exhibited a deviation $c = 0.25$ mm $\pm$ 0.12 mm; while, notched beams exhibited geometric deviation $c = 0.11$ mm $\pm$ 0.08 mm. Simple beams and beams with notches also exhibited inaccurate boundary profile at the base of the printing plane. Cantilever samples did not exhibit appreciable geometric deviation.

3.3. Mechanical tests

Simple beams were subjected to three point bending (3PBT, $N = 25$) and to four point bending tests (4PBT, $N = 5$). These samples resulted unsuitable for bending tests due to the edge imperfections due to backlight exposition. The loading points and the support were directly acting on the inaccurate edge, resulting from the printing process. This resulted in a highly compliant system which resulted in an elastic modulus of $E_f = 25.7$ GPa$\pm$7.9 GPa which was a large underestimate of the expected value; furthermore, a wide scattering of data was found. The flexural strength was 77.0 MPa $\pm$ 20 MPa.

The notched beams were used for flexural strength assessment only. The combination of the maximum force measured on each sample and the application of (1) resulted in an average strength of 135 MPa $\pm$ 58.6 MPa.

Cantilever samples exhibited an average elastic modulus of 98.2 GPa with a standard deviation of 22.4 GPa. The average strength was 115.1 MPa $\pm$ 37.0 MPa.

Starting from a surface roughness of $R_a = 254$ nm $\pm$ 31 nm and $R_q = 315$ nm $\pm$ 37 nm, the surface finishing performed after embedding the samples in the resin resulted in a surface roughness of $R_a = 55$ nm$\pm$ 23 nm and $R_q = 87$ nm $\pm$ 29 nm.

Berkovich indentation tests have shown an elastic behavior of the material not significantly dependent on the applied load. Fig. 8 shows the reduced modulus at different applied indentation loads.

Pooling all results collected at different loads, the average reduced modulus was 100.1 GPa $\pm$ 24.0 GPa. The Young modulus of the material E_s was estimated by solving the relationships (4) and (5) for E_s and assuming a Poisson coefficient of the hydroxyapatite $\nu_s = 0.28$; the average Young modulus was 101.7 GPa $\pm$ 27.3 GPa.

The Mann Whitney U tests has shown that the average values of elastic modulus obtained through the nanoindentation testing and that obtained through the cantilever bending are not significantly different (p-value = 0.34). Fig. 9 shows the median values of the elastic moduli as obtained through the nanoindentation tests and the bending of cantilever samples; cross symbols represent outliers.

Fig. 10 shows the median values and outliers of strength as obtained on cantilever and notched samples.

The Mann Witney U test has shown that the flexural strength obtained through the bending of notched beams and cantilevers did not show any statistically significant difference ($p = 0.4$); while the flexural strength as obtained through the bending of simple beams (pooling together the 3PBT and the 4PBT) was significantly lower than to those adopted/found in for cantilever and notched beams ($p = 1.5 \cdot 10^{-4}$ and $p = 8 \cdot 10^{-6}$), respectively.

Fig. 11 shows the Weibull diagram collected from all strength data. A Weibull modulus $m = 2.6$ and a shape factor of 143 MPa were found.

4. Discussion

The aim of this paper was to provide a mechanical characterization of the HAP obtained through VPP; in particular, the samples were designed and printed with characteristic size (less than half mm) similar to that of a typical trabecular structure in HAP-based bone tissue engineering scaffolds (Baino et al., 2022) fabricated according to analogous process and sintering treatment. To this purpose, after a

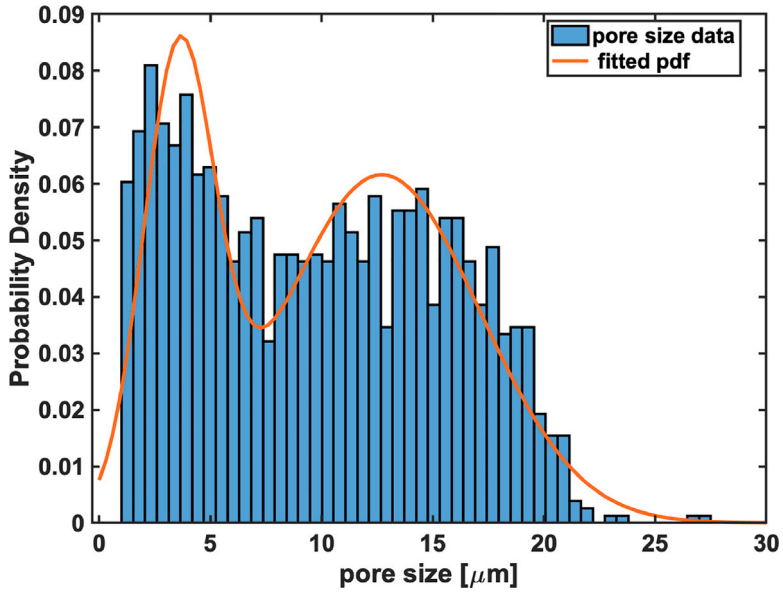

Fig. 6. Histogram of pore diameter as obtained from micro-CT data analysis; red lines refer to a bi-modal normal distribution.

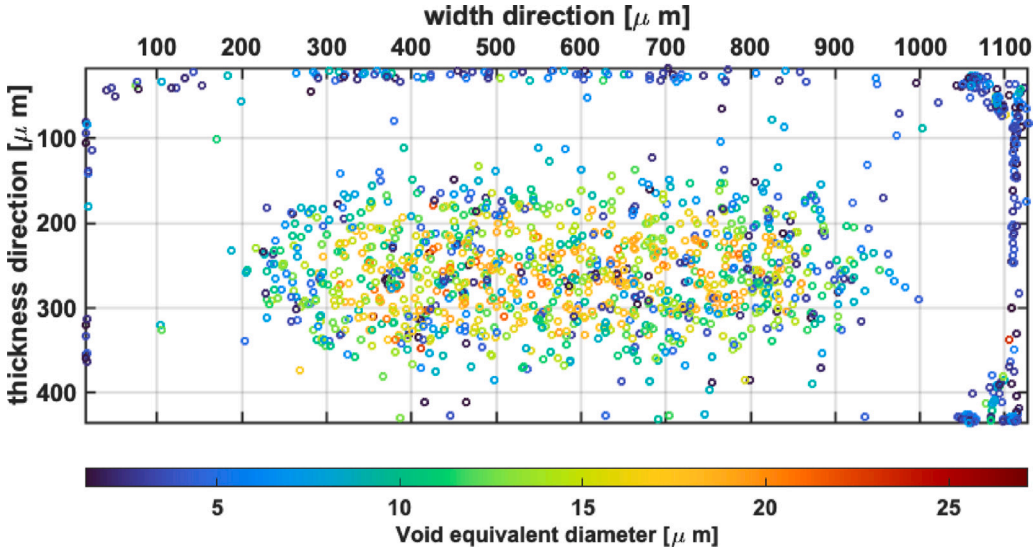

Fig. 7. Spatial distribution of pores, color map refers to pore diameter [μm].

Table 2
Geometric size of samples produced through vat photopolymerization.

Type	L [mm]	w [mm]	t [mm]	R [mm]	t_{res} [mm]
beams (nominal)	10	1	0.4	–	–
beams (measured)	9.68 ± 0.05	1.02 ± 0.2	0.47 ± 0.02	–	–
beams w. notch (nominal)	10	1	0.4	0.2	0.2
beams w. notch (measured)	9.69 ± 0.03	0.97 ± 0.04	0.50 ± 0.03	0.25 ± 0.05	0.31 ± 0.04
cantilever (nominal)	7	1	0.4	–	–
cantilever (measured)	6.60 ± 0.03	0.98 ± 0.02	0.35 ± 0.02	–	–

preliminary geometric characterization of the samples, through micro-CT and confocal laser scanning, mechanical tests were performed, namely micro-bending tests and nanoindentation.

The elastic moduli determined by nanoindentation tests and micro-bending tests yielded consistent results; likewise, the strength values determined with three different sample types were consistent, proving the validity of the mechanical properties determined and the soundness of the experimental setup. To the best of the Authors' knowledge, this is the first work presenting results on small size HAP samples obtained by VPP. Singh et al. (2021) characterized HAP fabricated by material extrusion using dog-bone samples with the smallest size as large as 4 mm. In Liu et al. (2021), whole HAP scaffolds have been characterized while intrinsic material properties of the constituent HAP was not determined. Mechanical characterization of samples by VPP is

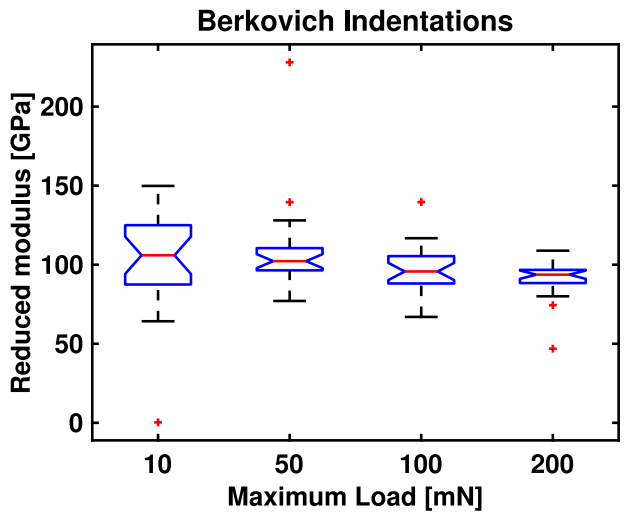

Fig. 8. Reduced modulus of HAP samples obtained through Berkovich indentations at different applied loads.

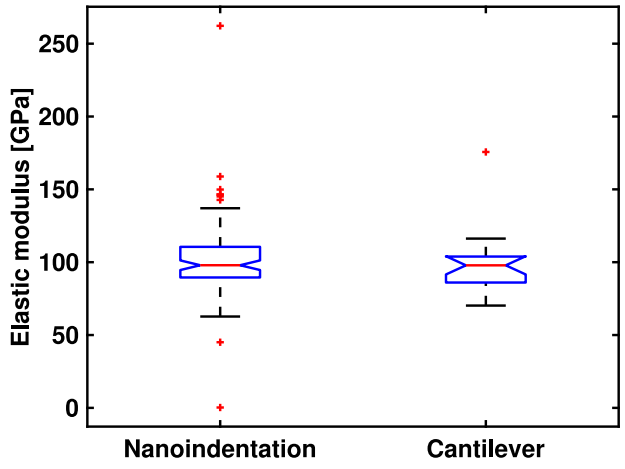

Fig. 9. Median values of Young modulus as obtained through nanoindentation testing and bending of cantilevers, outliers are reported with cross symbols.

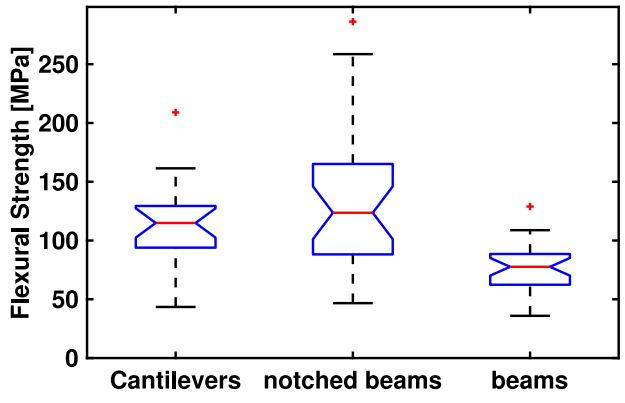

Fig. 10. Median values of flexural strength as obtained through bending of cantilevers, notched beams and simple beams; outliers are reported with cross symbols.

available in Schlacher et al. (2020); here alumina samples fabricated by VPP are characterized; the smallest size investigated was 2 mm, which is substantially larger than that analyzed in this work.

The micro-CT analyses and the confocal laser scanning revealed a highly dense material with a negligible residual porosity (approx. 0.35%), which demonstrates the effectiveness of the printing and sintering processes. The geometrical characterization of porosity is limited by the spatial resolution of the micro-CT images which was 0.9 μm, thus leaving unrevealed potential nano-porosity of the material; furthermore, the pores with characteristic size close to spatial resolution of the images might also be affected by noise and analysis artifacts; however, the average micro-pore size and the overall micro-porosity found are reliable. The estimated intrinsic porosity found in VPP manufactured HAP was comparable to than found in other additively manufactured ceramics. However, it is worth underlining that the HAP samples fabricated by VPP in this work are sintered pressurlessly. In Porwal et al. (2013) less than 1% porosity is achieved after 50 MPa post-production compression; Rapacz-Kmita et al. (2006) obtained $HAP-ZrO_2$ samples with 50% porosity in pressure-less conditions, while lower porosity was achieved by the hot pressing method. Similarly, Wang et al. (2019) applied the hot-pressing technique to obtain low porosity alumina samples. However, the density of the HAP samples produced in this work (around 99.7%) is comparable – and in some cases even higher – to that of high-density materials investigated in the above-cited studies.

Deviation from nominal geometry was in general within the 17% error with the exception of the error on the t_{res} parameter for which a 100 μm error was found, which is approximately 50% of t_{res}. However, it is worth noticing that the t_{res} parameter was the thinnest features of the sample (200 μm); furthermore, part of this error is also owed to the imperfection of the basal printing plane. This particular problem was not found on the cantilever samples; this is due to the fact that these latter were printed vertically, differently from the beams which were printed horizontally. The imperfections on the basal printing planes did not allow determining reliable estimates of the elastic modulus on beams.

Some of the beams (simple and notched beams) also exhibited a non rectilinear longitudinal axes; this deviation is owed to differential shrinkage during cooling.

The overall elastic modulus of the material was successfully determined through the bending of cantilever samples. Furthermore, the elastic modulus assessed through the nanoindentation tests was the same (statistically) as that obtained from bending of cantilever, thus confirming that the minimal residual porosity does not have any significant effect on the overall elastic modulus of the material.

The flexural strength was assessed mainly through the 4PBT of notched samples and on bending of cantilevers. The strength obtained through these two kinds of tests were statistically the same; this indicates that the printing defects found on the basal printing plane of the notched beams, although having a relevant effect on stiffness (addition compliance on the whole bending system), had no significant effect on the overall strength of the HAP. Possible mechanical anisotropy of samples was not specifically investigated in this study. A slight dependence of strength on orientation was reported for alumina samples produced through the same technology in a previous study (Schlacher et al., 2020). Looking at the final application addressed to HAP scaffolds, however, the problem of orientation-dependent anisotropy seems not to be relevant as scaffolds struts are printed along different orientations, thus yielding a homogeneization effect.

Although a consistent comparison of the elastic modulus and of the flexural strength with values available in literature is not possible as manufacturing process or nano-micro architectural features may differ with respect to that found in this study, some remarks can still be presented.

Miranda et al. (2007) has studied HAP scaffolds obtained through the robocasting technique. A Berkovich indentation study using an indentation force of 2 N revealed an elastic modulus of approximately 82 GPa (assumption is made of the Poisson ratio $\nu = 0.28$). This elastic modulus is lower than that found with the Berkovich indentation presented in this study. The HAP material shown in Miranda

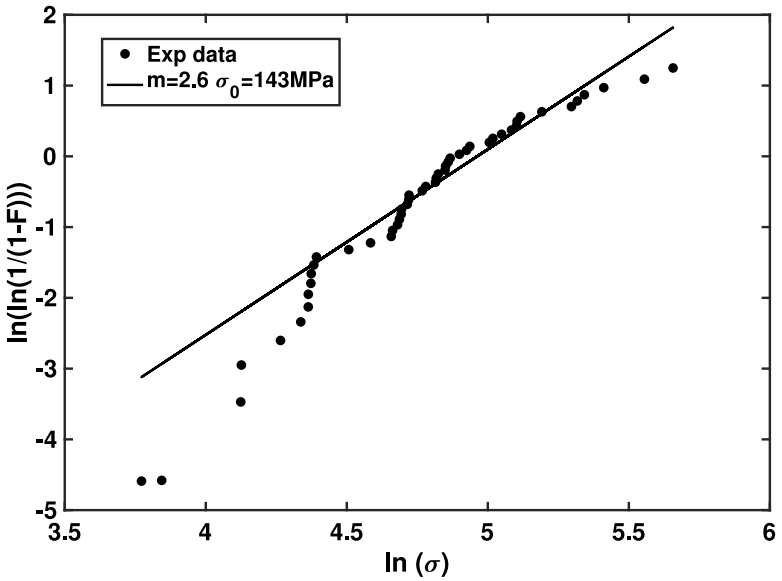

Fig. 11. Weibull parameters for flexural strength as obtained through bending of cantilever and from notched beams.

et al. (2007) exhibits an intrinsic porosity of approx. 15% which is substantially higher than that found in our study. Such an intrinsic porosity would justify the lower elastic modulus. Indeed, if a simple Mori–Tanaka scheme is used to determine the elastic modulus of a micro-porous material (section 7.3 in Qu and Cherkaoui (2007)), one would get at 15% porosity an elastic modulus of approximately $0.74 \cdot E_{bulk}$ (assumption on Poisson ratio for the bulk modulus $\nu = 0.28$ is made).

As in our study a fully dense HAP has been obtained (intrinsic porosity of about 0.3%), the elastic modulus found by Miranda et al. would bring to a fully dense material property which is $E_{bulk} = 82/0.74 = 110$ GPa, which is within the data range found in our study.

In another study by Zhang et al. (2022), VPP is used to produce porous HAP for bone regeneration devices. In this work only compressive strength was determined on cylindrical samples having 6.5 mm in diameter and 13 mm height and mass fraction between 50% and 70%; the compressive strength was between 19.75 MPa and 48.0 MPa. Comparison of these strength with that found in our study should be made with caution as compressive strength on macroscopic samples is obtained in Zhang et al. (2022) while flexural strength on micron-size samples is reported in our study. Furthermore, the sintering temperature adopted in our study was higher than that in Zhang et al. (2022) which was from 1015 °C to 1250 °C, thus implying a higher density with respect to that in Zhang et al..

In Ranito et al. (2006), fully dense P214S medical grade synthetic HAP blocks obtained from powder compression and sintering in a temperature range of 1150 °C to 1350 °C were characterized. At a sintering temperature similar to that used in the present study, Ranito et al. have found an open porosity of approximately 20% which is higher than that found in our samples; Ranito et al. have found an elastic modulus of 100 GPa ± 4 GPa, which is similar to that found in the present study, and a flexural strength of 68 MPa±8 MPa as measured on macroscopic rectangular bars ($50 \times 4.5 \times 3.5$ mm). The flexural strength reported by Ranito et al. is substantially lower than that found in the present study; this is most likely due to the higher compactness achieved through the VPP of this study. Because no statistical difference in strength was found between the notched beams and the cantilever samples, the Weibull parameters for the entire set of results were estimated; a Weibull modulus of 2.6 was found (see Fig. 11). No consistent comparison with other works can be done for the Weibull modulus; indeed, Fan et al. (2013) found Weibull parameters higher (between 6 and 15) than that found in this study; however, the samples were obtained through a different manufacturing process (powder compression and sintering) which eventually resulted in a higher Weibull modulus. The low Weibull modulus found in the present work is mainly owed to geometrical imperfections of the samples; indeed, strength of the cantilevers only, which exhibited a more accurate geometry, was slightly higher ($m = 3.4$, N = 20); while the Weibull modulus for the notched beams only was $m = 2.5$, N = 29. The Weibull modulus can be increased by post-sintering surface machining which eliminates or strongly reduces surface defects, as shown by Schlacher et al. (2020) in VPP-produced alumina samples; however, this approach is not relevant for bone scaffold applications as mechanical finishing of the surfaces in a three-dimensional porous scaffold would not be possible. A substantial increase of the Weibull modulus might be achieved through improvement of printing fidelity reducing geometric size variability in the sample population and reducing the geometric imperfections highlighted in this study.

A further approach which may lead to the Weibull modulus improvement is the optimization of the sintering process which may lead to reduced intrinsic porosity; though this would bring to a marginal improvement of the Weibull modulus as intrinsic porosity found in the HAP samples is very low compared to other sintering-based manufacturing processes.

HAP scaffolds obtained through VPP in Baino et al. (2022), under analogous processing/sintering conditions than those applied in the present study for fabricating bulk samples underwent to uniaxial compressive tests and exhibited a Weibull modulus of 2.2, which is consistent with that reported in this study. This comparison should, however, be done with caution, as complex architecture of the scaffolds may imply defects in the structures which are not occurring in the simple geometries considered in this paper.

As the Weibull modulus obtained so far on solid HAP samples (this study) and on scaffolds (Baino et al., 2022) is very low in comparison to other ceramics obtained using the same technology (see for example alumina samples in Schlacher et al. (2020)), the application of VPP to bone scaffolds necessitates appropriate design approaches that optimize the mechanical performances of the scaffolds depending on the anatomical location of the implant and on a reliable lower threshold of the solid material strength.

5. Conclusions

Three-dimensional AM technologies are constantly growing, opening a virtually unbounded space to design complex architectures for

implants and devices. The biomedical industry and the bone tissue engineering, in particular, are taking great advantage of these new opportunities.

Each technology produces materials with different intrinsic properties; therefore, an accurate knowledge of the intrinsic material properties resulting from a specific technology and for characteristic size which are the same of the final product is greatly relevant for a reliable design of devices. To the authors' knowledge, this is the first work in which mechanical and geometrical properties of HAP obtained through a AM technology have been assessed by testing small sized samples having the same characteristic size as that of the final application in bone tissue engineering scaffolds. Askari et al. (2020) emphasize the need to determine mechanical properties of the solid phase in a ceramic scaffold by testing the material at the scale of the microstructures as these properties are considerably different with respect to that of the material manufactured at larger size. In particular, in Askari et al. (2020) only the elastic modulus was assessed at the small scale by means of nanoindentation on zirconia scaffold obtained though the foam replication technique.

This work provides a detailed assessment of the geometrical features and mechanical properties of HAP obtained through VPP for a given set of manufacturing parameters. In particular, dimensional fidelity and deviation from ideal geometry were quantitatively assessed, as well as the main mechanical properties through complementary methods. Micro-porosity was also quantified through high resolution Computed micro-Tomography analyses. This study has shown that the VPP can manufacture high quality HAP with remarkable elastic modulus and strength. The acquired information are relevant when approaching a rational design of BTE scaffolds.

CRediT authorship contribution statement

Luca D'Andrea: Writing – review & editing, Writing – original draft, Software, Investigation, Formal analysis, Data curation. **Dario Gastaldi:** Investigation. **Francesco Baino:** Writing – review & editing, Investigation. **Enrica Verné:** Writing – review & editing, Investigation. **Giulia Saccomano:** Writing – review & editing, Investigation. **Lorenzo D'Amico:** Writing – review & editing, Investigation. **Elena Longo:** Writing – review & editing, Investigation. **Martin Schwentenwein:** Writing – review & editing, Investigation. **Pasquale Vena:** Writing – review & editing, Writing – original draft, Supervision, Methodology, Funding acquisition, Data curation, Conceptualization.

Declaration of competing interest

The authors declare that they have no known competing financial interests or personal relationships that could have appeared to influence the work reported in this paper.

Data availability

Data will be made available on request.

Acknowledgment

The student Carlotta Dall'Agata is kindly acknowledged for performing part of the experiments.

Dr. Giuliana Tromba from the "Elettra-Sincrotrone" facility in Trieste is also kindly acknowledged for her support in carrying out the Computed micro-Tomography scans.

The "Elettra-Sincrotrone" facility in Trieste (Italy) is kindly aknowledged for allocating beamtime for this study.

References

Askari, E., Cengiz, I., Alves, J., Henriques, B., Flores, P., Fredel, M., Reis, R., Oliveira, J., Silva, F., Mesquita-Guimarães, J., 2020. Micro-CT based finite element modelling and experimental characterization of the compressive mechanical properties of 3-D zirconia scaffolds for bone tissue engineering. J. Mech. Behav. Biomed. Mater. 102, 103516. http://dx.doi.org/10.1016/j.jmbbm.2019.103516, URL https://www.sciencedirect.com/science/article/pii/S1751616119309944.

Baino, F., Magnaterra, G., Fiume, E., Schiavi, A., Tofan, L.-P., Schwentenwein, M., Verné, E., 2022. Digital light processing stereolithography of hydroxyapatite scaffolds with bone-like architecture, permeability, and mechanical properties. J. Am. Ceram. Soc. 105 (3), 1648–1657. http://dx.doi.org/10.1111/jace.17843, URL https://ceramics.onlinelibrary.wiley.com/doi/abs/10.1111/jace.17843.

Bigham, A., Foroughi, F., Ghomi, E.R., Rafienia, M., Neisiany, R.E., Ramakrishna, S., 2020. The journey of multifunctional bone scaffolds fabricated from traditional toward modern techniques. 3, pp. 281–306. http://dx.doi.org/10.1007/s42242-020-00094-4.

Brun, F., Pacilè, S., Accardo, A., Kourousias, G., Dreossi, D., Mancini, L., Tromba, G., Pugliese, R., 2015. Enhanced and flexible software tools for X-ray computed tomography at the Italian synchrotron radiation facility elettra. Fund. Inform. 141 (2–3), 233–243. http://dx.doi.org/10.3233/FI-2015-1273.

Campana, V., Milano, G., Pagano, E., Barba, M., Cicione, C., Salonna, G., Lattanzi, W., Logroscino, G., 2014. Bone substitutes in orthopaedic surgery: from basic science to clinical practice. J. Mater Sci. Mater Med 25, 2445–2461. http://dx.doi.org/10.1007/s10856-014-5240-2.

Chen, Q., Baino, F., Spriano, S., Pugno, N., Vitale-Brovarone, C., 2014. Modelling of the strength-porosity relationship in glass-ceramic foam scaffolds for bone repair. J. the Eur Ceramic Society 34 (11), 2663–2673. http://dx.doi.org/10.1016/j.jeurceramsoc.2013.11.041, URL https://www.scopus.com/inward/record.uri?eid=2-s2.0-84901253034&doi=10.1016%2fj.jeurceramsoc.2013.11.041&partnerID=40&md5=1292a534e9fd12944bf03a6252253203, cited By 36.

Dorozhkin, S.V., Epple, M., 2002. Biological and medical significance of calcium phosphates. Angewandte Chem. Int Edition 41 (17), 3130–3146, URL https://onlinelibrary.wiley.com/doi/abs/10.1002/1521-3773%2820020902%2941%3A17%3C3130%3A%3AAID-ANIE3130%3E3.0.CO%3B2-1.

Dullin, C., di Lillo, F., Svetlove, A., Albers, J., Wagner, W., Markus, A., Sodini, N., Dreossi, D., Alves, F., Tromba, G., 2021. Multiscale biomedical imaging at the SYRMEP beamline of elettra - closing the gap between preclinical research and patient applications. Physics Open 6, 100050. http://dx.doi.org/10.1016/j.physo.2020.100050, URL https://www.sciencedirect.com/science/article/pii/S2666032620300375.

Entezari, A., Roohani-Esfahani, S.-I., Zhang, Z., Zreiqat, H., Dunstan, C.R., Li, Q., 2016. Fracture behaviors of ceramic tissue scaffolds for load bearing applications. Sci. Rep. 6, 28816.

Fan, X., Case, E.D., Gheorghita, I., Baumann, M.J., 2013. Weibull modulus and fracture strength of highly porous hydroxyapatite. J. Mech. Behav. Biomed. Mater. 20, 283–295. http://dx.doi.org/10.1016/j.jmbbm.2013.01.031.

Farina, E., Gastaldi, D., Baino, F., Vernè, E., Massera, J., Orlygsson, G., Vena, P., 2021. Micro computed tomography based finite element models for elastic and strength properties of 3D printed glass scaffolds. Acta Mech. Sinica 37 (2), 292–306. http://dx.doi.org/10.1007/s10409-021-01065-3, URL http://dx.doi.org/10.1007/s10409-021-01065-3.

Gastaldi, D., Baleani, M., Fognani, R., Airaghi, F., Bonanni, L., Vena, P., 2020. An experimental procedure to perform mechanical characterization of small-sized bone specimens from thin femoral cortical wall. J. Mech. Behav. Biomed. Mater. 112, 104046. http://dx.doi.org/10.1016/j.jmbbm.2020.104046, URL https://www.sciencedirect.com/science/article/pii/S1751616120305956.

Ghorbani, F., Li, D., Ni, S., Zhou, Y., Yu, B., 2020. 3D printing of acellular scaffolds for bone defect regeneration: A review. Mater. Today Commun. 22, 100979. http://dx.doi.org/10.1016/j.mtcomm.2020.100979, URL https://www.sciencedirect.com/science/article/pii/S2352492819306245.

Goloshchapov, D., Lenshin, A., Savchenko, D., Seredin, P., 2019. Importance of defect nanocrystalline calcium hydroxyapatite characteristics for developing the dental biomimetic composites. Results Phys. 13, 102158. http://dx.doi.org/10.1016/j.rinp.2019.102158, URL https://www.sciencedirect.com/science/article/pii/S221137971930155X.

Jiao, C., Xie, D., He, Z., Liang, H., Shen, L., Yang, Y., Tian, Z., Wu, G., Wang, C., 2022. Additive manufacturing of bio-inspired ceramic bone scaffolds: Structural design, mechanical properties and biocompatibility. Materials Design 217, 110610. http://dx.doi.org/10.1016/j.matdes.2022.110610, URL https://www.sciencedirect.com/science/article/pii/S0264127522002313.

Kim, C., Lee, J.W., Heo, J.H., Park, C., Kim, D.-H., Yi, G.S., Kang, H.C., Jung, H.S., Shin, H., Lee, J.H., 2022. Natural bone-mimicking nanopore-incorporated hydroxyapatite scaffolds for enhanced bone tissue regeneration. Biomater Res 26 (1), 7. http://dx.doi.org/10.1186/s40824-022-00253-x, URL http://dx.doi.org/10.1186/s40824-022-00253-x.

Kumar, A., Kargozar, S., Baino, F., Han, S.S., 2019. Additive manufacturing methods for producing hydroxyapatite and hydroxyapatite-based composite scaffolds: A review. Front. Mater. 6, http://dx.doi.org/10.3389/fmats.2019.00313, URL https://www.frontiersin.org/article/10.3389/fmats.2019.00313.

Liu, R., Ma, L., Liu, H., Xu, B., Feng, C., He, R., 2021. Effects of pore size on the mechanical and biological properties of stereolithographic 3D printed HAp bioceramic scaffold. Ceram. Int. 47 (20), 28924–28931. http://dx.doi.org/10.1016/j.ceramint.2021.07.053, URL https://www.sciencedirect.com/science/article/pii/S0272884221020800.

Miranda, P., Pajares, A., Saiz, E., Tomsia, A.P., Guiberteau, F., 2007. Fracture modes under uniaxial compression in hydroxyapatite scaffolds fabricated by robocasting. 83A, 646–655. http://dx.doi.org/10.1002/jbm.a.31272.

Otsu, N., 1979. A tlreshold selection method from gray-level histograms. IEEE Trans Syst, Man, Cybern SMC-9 (1), 62–66.

Paganin, D., Mayo, S.C., Gureyev, T.E., Miller, P.R., Wilkins, S.W., 2002. Simultaneous phase and amplitude extraction from a single defocused image of a homogeneous object. J. Microsc. 206 (1), 33–40. http://dx.doi.org/10.1046/j.1365-2818.2002.01010.x, URL https://onlinelibrary.wiley.com/doi/abs/10.1046/j.1365-2818.2002.01010.x.

Paterlini, A., Stamboulis, A., Turq, V., Laloo, R., Schwentenwein, M., Brouczek, D., Piccinini, M., Bertrand, G., 2021. Lithography-based manufacturing of advanced ceramics for orthopaedic applications: A comparative tribological study. Open Ceramics 8, http://dx.doi.org/10.1016/j.oceram.2021.100170, URL https://www.scopus.com/inward/record.uri?eid=2-s2.0-85122767793&doi=10.1016%2fj.oceram.2021.100170&partnerID=40&md5=1595f49dad16aadaea125325be570971, Cited by: 0; All Open Access, Gold Open Access, Green Open Access.

Porwal, H., Tatarko, P., Grasso, S., Khaliq, J., Dlouhý, I., Reece, M.J., 2013. Graphene reinforced alumina nano-composites. Carbon 64, 359–369. http://dx.doi.org/10.1016/j.carbon.2013.07.086, URL https://www.sciencedirect.com/science/article/pii/S0008622313007203.

Qu, J., Cherkaoui, M., 2007. Fundamentals of Micromechanics of Solidss. pp. 1–386. http://dx.doi.org/10.1002/9780470117835, URL https://www.scopus.com/inward/record.uri?eid=2-s2.0-84889447904&doi=10.1002%2f9780470117835&partnerID=40&md5=70af9798c151a13dc0f233ea8eae40a7, Cited by: 289,

Ranito, C., Costa Oliveira, F., Borges, J., 2006. Mechanical characterization of dense hydroxyapatite blocks. Materials Science Forum 514–516 (PART 2), 1083–1086. http://dx.doi.org/10.4028/www.scientific.net/msf.514-516.1083, URL https://www.scopus.com/inward/record.uri?eid=2-s2.0-37848999017&doi=10.4028%2fwww.scientific.net%2fmsf.514-516.1083&partnerID=40&md5=9004d5ec6f8c0392610b398f4ab5df12, cited By 1.

Rapacz-Kmita, A., Ślósarczyk, A., Paszkiewicz, Z., 2006. Mechanical properties of HAp–ZrO2 composites. J. the Eur Ceramic Society 26 (8), 1481–1488. http://dx.doi.org/10.1016/j.jeurceramsoc.2005.01.059, URL https://www.sciencedirect.com/science/article/pii/S0955221905001329.

Ritchie, R.O., 2011. The conflicts between strength and toughness. Nature Mater. 10, 817–822. http://dx.doi.org/10.1038/nmat3115.

Schlacher, J., Lube, T., Harrer, W., Mitteramskogler, G., Schwentenwein, M., Danzer, R., Bermejo, R., 2020. Strength of additive manufactured alumina. J. the Eur Ceramic Society 40 (14), 4737–4745. http://dx.doi.org/10.1016/j.jeurceramsoc.2020.03.073, URL https://www.sciencedirect.com/science/article/pii/S0955221920302545, Fractography of Advanced Ceramics VI.

Shahgholi, M., Oliviero, S., Baino, F., Vitale-Brovarone, C., Gastaldi, D., Vena, P., 2016. Mechanical characterization of glass-ceramic scaffolds at multiple characteristic lengths through nanoindentation. J. the Eur Ceramic Society http://dx.doi.org/10.1016/j.jeurceramsoc.2016.01.042, URL http://www.sciencedirect.com/science/article/pii/S0955221916300425.

Singh, R., Singh, G., Singh, J., Kumar, R., 2021. Investigations for tensile, compressive and morphological properties of 3D printed functional prototypes of PLA-PEKK-HAp-CS. J. Thermoplastic Composite Mater 34 (10), 1408–1427. http://dx.doi.org/10.1177/0892705719870595, URL http://dx.doi.org/10.1177/0892705719870595.

Szcześ, A., Hołysz, L., Chibowski, E., 2017. Synthesis of hydroxyapatite for biomedical applications. Adv. Colloid Interface Sci. 249, 321–330. http://dx.doi.org/10.1016/j.cis.2017.04.007, URL https://www.sciencedirect.com/science/article/pii/S0001868617300957, Recent nanotechnology and colloid science development for biomedical applications.

Wang, X., Zhao, J., Cui, E., Liu, H., Dong, Y., Sun, Z., 2019. Effects of sintering parameters on microstructure, graphene structure stability and mechanical properties of graphene reinforced Al2O3-based composite ceramic tool material. Ceram. Int. 45 (17, Part B), 23384–23392. http://dx.doi.org/10.1016/j.ceramint.2019.08.040, URL https://www.sciencedirect.com/science/article/pii/S0272884219322357.

Zeng, Y., Yan, Y., Yan, H., Liu, C., Li, P., Dong, P., Zhao, Y., Chen, J., 2018. 3D printing of hydroxyapatite scaffolds withgood mechanical and biocompatible properties by digital light processing. J. Mater. Sci. 53 (9), 6291–6301. http://dx.doi.org/10.1007/s10853-018-1992-2, URL http://dx.doi.org/10.1007/s10853-018-1992-2.

Zhang, B., Gui, X., Song, P., Xu, X., Guo, L., Han, Y., Wang, L., Zhou, C., Fan, Y., Zhang, X., 2022. Three-dimensional printing of large-scale, high-resolution bioceramics with micronano inner porosity and customized surface characterization design for bone regeneration. ACS Appl. Mater. Interfaces 14, 8804–8815. http://dx.doi.org/10.1021/acsami.1c22868.

Zocca, A., Colombo, P., Gomes, C.M., Günster, J., 2015. Additive manufacturing of ceramics: Issues, potentialities, and opportunities. J. Am. Ceram. Soc. 98 (7), 1983–2001. http://dx.doi.org/10.1111/jace.13700, URL https://ceramics.onlinelibrary.wiley.com/doi/abs/10.1111/jace.13700.